RSC Advances

PAPER

View Article Online
View Journal | View Issue

Cite this: *RSC Adv.*, 2022, **12**, 1663

Effects of zinc–aluminium injection on corrosion behaviour and semiconductor properties of carbon steel in the PHT system of PHWR

Yang Jiao,[ab] Shenghan Zhang *[ab] and Yu Tan[ab]

Received 27th October 2021
Accepted 24th December 2021

DOI: 10.1039/d1ra07921b

rsc.li/rsc-advances

Carbon steel is widely used as the piping of the primary heat transport system (PHT) in pressurized heavy water reactors (PHWR). Effects of zinc/aluminum treatment and simultaneous injection of zinc and aluminum on corrosion behavior and semiconductor properties of oxide films formed on carbon steels were characterized by the gravimetric method, potentiodynamic polarization scan, EIS, Mott–Schottky test, SEM, EDS mapping, XPS analysis and photocurrent response measurement. The results showed that all the metal cation ions treatment can improve the corrosion resistance of oxide films in varying degrees. 20 ppb Zn^{2+} had the greatest enhancement in corrosion resistance, followed by 20 ppb Zn^{2+} + 20 ppb Al^{3+}. $ZnFe_2O_4$, $FeAl_2O_4$ and $ZnAl_2O_4$ were detected to be new spinel phases generated in oxide films. The oxide films on the surface of carbon steel all demonstrated n-type semiconductor properties. It was worth noting that the total content of manganese and zinc in the oxide film played an important role in the corrosion resistance of carbon steel.

1 Introduction

CANDU pressurized heavy water reactors (PHT) which use heavy water (D_2O) as the moderator are operated in Canada, Korea, China, India and many other countries. The primary heat transport (PHT) system is the core system of the primary circuit in PHWR. D_2O is circulated through this circuit using primary coolant pumps. Most of the PHT piping and feeder pipes and related reactor designs are fabricated from carbon steel (CS), ASTM A106 Gr-B or ASTM A 333 Gr-6.[1–6]

In nuclear power plants, water chemistry of the coolant is carefully monitored and controlled for the integrity of the system structure.[7,8] Although CANDU design is significantly different from that of light water reactors (LWR), many materials corrosion and degradation issues are equally important and directly affect the safety of reactor operation. Carbon steel pipes corrode during the high temperature (inlet and outlet temperature being 266 °C to 310 °C) and high pressure in long-time operation. Therefore, to reduce the corrosion of carbon steel and prevent local deposition of corrosion products, an alkaline $pH_{25\ °C}$ of 10.2–10.6 is maintained by the addition of lithium hydroxide (LiOH) in the reactor primary circuit.[4,9–11]

It has been reported that the composition and grain boundaries of alloys could be modified to improve their corrosion resistance.[12] Zinc injection technology has been widely used in the primary circuit coolant of nuclear power plants. It is generally considered that the addition of zinc into the coolant can retard the corrosion rate of metal materials and reduce the buildup of radiation field and the occupational radiation dose.[13]

Many studies have reported that the compact oxide layer and high corrosion resistance of carbon steel could be obtained due to the generation of zinc ferrite ($ZnFe_2O_4$) oxide. Sawicki's research identified the effects of 15–60 ppb soluble zinc on the surface composition of carbon steel in primary-side coolant by using conversion and electron and X-ray backscattering Mössbauer spectroscopy. High electrical resistivity zinc ferrite was formed on coupons when exposed to zinc added solution. A layer of zinc ferrite in the oxide film played an important role in reducing corrosion products release rates.[14] Walker Z. H. pointed that in the presence of 15 ppb zinc only a slight reduction was found in corrosion of CS coupons. Moreover, zinc ferrite showed a significantly lower thermal conductivity than without zinc addition and reduced the heat transfer efficiency in the primary circuit.[15]

However, ^{64}Zn in natural zinc was easily irradiated by neutrons to produce high radioactive ^{65}Zn, expensive depleted zinc was used in nuclear power plants. ^{27}Al is a stable nuclide and have no radioactive. Aluminium ion is a good corrosion inhibitor which has been widely applied in industrial cooling water. Previous studies have addressed the influence of zinc and aluminium simultaneous injection on corrosion behaviours of stainless steels in simulated PWR primary circuit environments.[16–18]

[a]*Hebei Key Lab of Power Plant Flue Gas Multi-Pollutants Control, Department of Environmental Science and Engineering, North China Electric Power University, Baoding, 071003, China. E-mail: shenghan_zhang@126.com*

[b]*Environmental System Optimization, College of Environmental Science and Engineering, North China Electric Power University, Beijing, 102206, China*

The aim of this study was to evaluate the effect of zinc and/or aluminum added into simulated primary circuit coolant of heavy water reactors. The oxide films on carbon steels were formed in high temperature and high pressure solutions. After oxidation for 168 h, the corrosion behavior and semiconductor properties of samples were analyzed by potentiodynamic polarization scan, electrochemical impedance spectroscopy (EIS), and Mott–Schottky curve. The morphology of carbon steel surface was measured by scanning electronic microscopy (SEM). The composition of oxide films were analyzed by photocurrent response, energy dispersive spectrometer (EDS) mapping and X-ray photoelectron spectroscopy (XPS).

2 Experimental methods

2.1 Materials

The carbon steel of ASTM A106-Grade B (20$^{\#}$ in Chinese label) was used in this experiment. Experimental specimens were cut into small pieces of 12 × 12 × 2 mm and punched a role with the diameter of 1.5 mm in the upper left corner. Prior to oxidation experiments, for uniform surface roughness of materials, every sample was mechanically polished step by step with 400, 800, 1200, and 1500 grit silicon carbide (SiC) metallurgical papers, rinsed with deionized water and degreased with ethanol thoroughly. Finally, A106B CS coupons were dried under a cold airflow, weighed (as the value of m_0 before oxidation used for gravimetric method in eqn (1)), and stored in a vacuum glass desiccator for further experiments.

2.2 Oxidation in simulated environment

The carbon steel specimens were arranged in a stainless steel static autoclave and exposed to high temperature (290 ± 1 °C) and high pressure (7.5 MPa) simulated PHT system conditions for 168 h. Lithium hydroxide was added into deionized water to adjust $pH_{25\ ^\circ C}$ in the range of 10.1–10.2 and was used as blank solution. The compositions of simulated test solution were shown in Table 1. Zinc acetate and aluminum acetate were selected in this experiment to provide Zn^{2+} and Al^{3+}. Every group included 10 parallel samples. After oxidation, when cooling down to the room temperature naturally, all coupons were taken out of autoclave, cleaned with deionized water, dried with cold wind, weighed (used for the value of m_1 after oxidation in eqn (1) to calculate the corrosion rate by gravimetric method) and finally kept in a vacuum desiccator.

Table 1 Composition of simulated test solution

Test solution	Li^+ (ppm)	Zn^{2+} (ppb)	Al^{3+} (ppb)
T (blank)	1	0	0
T (20Zn)	1	20	0
T (40Zn)	1	40	0
T (30Al)	1	0	30
T (20Zn + 20Al)	1	20	20

2.3 Electrochemical measurements

A standard three-electrode system in a 450 mL electrochemical cell was designed for electrochemical measurements. The surface of 0.2826 cm^2 on the specimens exposed to the test solution was used as working electrode, while a platinum electrode was the auxiliary electrode and a saturated calomel electrode (SCE) for the reference electrode. The electrolyte solution was 1 ppm LiOH solution. Two holes were set up for the inlet and outlet gas. Nitrogen gas was bubbled through the solution for about 30 min before all the tests.

Potentiodynamic polarization scan and electrochemical impedance spectroscopy (EIS) were carried out with CHI650D electrochemical workstation of Shanghai Chenhua Ltd at room temperature. Firstly, the open circuit potential (OCP) which unit was volts (V) was measured and monitored. The OCP value was determined in a stable state based on the changes in OCP value were less 10 mV within one minute. The actual entire immersion time from electrode immersion to stability state did not exceed 10 minutes. Then, the scanning range of potentiodynamic polarization were performed from −1.0 V to 0.8 V with respect to OCP at a scan rate of 0.001 V s^{-1}. EIS was measured at OCP with a frequency from 10^6 Hz to 10^{-2} Hz with the sinusoidal voltage of ±10 mV on the oxide films. Finally, the electrical parameters and fitting of the spectra were done by an equivalent electrical circuit using ZSimpwin software. Mott–Schottky curve were carried out with PARSTAT2273 potentiostat of Princeton Ltd in three-electrode cell. The potential range of test was −1000 mV to +1200 mV with a potential step of 0.01 V.

The photocurrent responses were performed by focusing a monochromatic modulated light through the quartz window on to the oxide films. A xenon lamp (350 W, Crownetch) with a grating monochromator (1/8 m, CT110, Crowntech) was used as the light source. The wavelength of lights ranged from 200 nm to 800 nm in steps of 10 nm. Before the experiments, the light intensity of different wavelength was measured by connecting a Si-photodiode to a digital ammeter positioned in the same place of the coupon. The photocurrent response value of the oxide films at different wavelength were mathematically transformed to attain the data with the change of photo energy.

2.4 Morphology and composition analysis of oxide films

After 168 h oxidation, the surface of oxide films was characterized by SEM and EDS mapping. HITACHI S4800 was used for the morphology analysis of oxide films with an accelerating voltage of 15.0 kV under different magnifications. The chemical states of main elements on the surface were analysis by XPS.

3 Results

3.1 Gravimetric method

The gravimetric method evaluates the degree of metal corrosion according to the weight change before and after corrosion. It is one of the commonly used methods in corrosion experiments of metals, and it can directly reflect the corrosion rate.

The corrosion rate of carbon steel in high temperature solution was calculated by eqn (1):

$$v = \frac{K(m_1 - m_0)}{StD} \quad (1)$$

where v is the corrosion rate (g mm^{-2} d^{-1}), K is a constant for unit conversion (in this study $K = 2.4 \times 10^6 \times D$ when the unit of v is mg dm^{-2} d^{-1}), m_1 is the weight of sample after oxidation (g), m_0 is the weight of sample before oxidation (g), S is the surface area of sample (mm^2), t is experimental time (d), D is density of metal (g cm^{-3}). Corrosion rates of carbon steel coupons in different conditions were shown in Table 2 and the standard deviation of each group calculated by eqn (2) was listed.

$$\sigma = \sqrt{\frac{\sum d^2}{n-1}} = \sqrt{\frac{\sum (m_i - \overline{m})^2}{n-1}} \quad (2)$$

where σ is the standard deviation, m_i is the measured value of each group, $\bar{m}$ is the average value of weight, n is the total number of group ($n = 10$).

It can be seen from the calculated results that with the injection of zinc and/or aluminum the corrosion rate of carbon steel decreased compared to T (blank). Samples in 20 ppb Zn^{2+} solution showed better corrosion resistance than that in high concentration of Zn^{2+}. T (20Zn + 20Al) had the slowest corrosion rate (half of T (blank)) which implied the best corrosion resistance of oxide film, but the reduction effect of zinc–aluminum injection was not significant.

3.2 Potentiodynamic polarization

The potentiodynamic polarization curves of oxide films formed on carbon steels with different concentration of zinc and aluminum were measured in 1 ppm LiOH solution at room temperature and were shown in Fig. 1. The intersection of anodic and cathodic Tafel lines determined the corrosion current density (i_{corr}) and corrosion potential (E_{corr}) and the results were listed in Table 3.

The high corrosion resistance in absence and presence of Zn^{2+} and Al^{3+} is attributed to protective nature of the passive film. From the data shown in Table 3, compared with blank group, the lower i_{corr} values for all the oxide samples were indicative of the better corrosion resistance. It was obvious that i_{corr} of T (20Zn) and T (20Zn + 20Al) showed an order of magnitude lower than other groups, and the open circuit potential (OCP) shifted toward to the noble side (−0.118 V and −0.348 V *vs.* SCE) compared carbon steel in blank group (−0.531 V *vs.* SCE). However, with sole injection of aluminum, i_{corr} showed little decrease than T (blank), which result in little

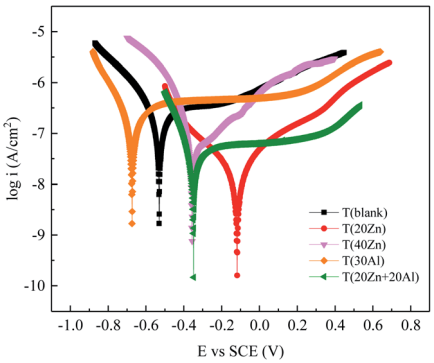

Fig. 1 Polarization curves of oxide films formed on CS in different solutions at 290 °C.

effect on the improvement of corrosion resistance. Consequently, among the different concentration of solution, 20 ppb Zn^{2+} was the most effective for improving the corrosion resistance of carbon steel in heavy water reactor water conditions.

3.3 Electrochemical impedance spectroscopy

Electrochemical impedance spectroscopy (EIS), which also called AC impedance, is commonly used to investigate the corrosion behavior of alloys and explain the structure of passive films formed on the metal surface.

EIS measurements were carried out for all samples in 1 ppm LiOH solution at room temperature. The Nyquist, phase angle and Bode plots of oxide films formed on carbon steel coupons in high temperature water with different concentration of zinc and aluminum were shown in Fig. 2(a), (b) and (c) respectively. For clearer comparison, Bode plots at low frequencies were shown in Fig. 2(d).

Two semicircles seen in Fig. 2(a) Nyquist diagram indicated the presence of two time constants attributed to process occurring near oxide/solution interface and oxide/metal interface after carbon steels exposed to high temperature water. The Bode spectra (Fig. 2(c) and (d)) showed a significant increase of impedance modulus at low frequencies after zinc and zinc + aluminum injected in the solution, especially for T (20Zn) which demonstrated the highest value of Z in the lowest frequency. The Bode plots of T (30Al) were almost coincide with T (blank), only a little lower than T (blank) when frequency less than 0.25 Hz, which indicated these two groups had similar corrosion resistance.

Table 2 Corrosion rates in different conditions

Group	Corrosion rate (g mm^{-2} d^{-1})	Standard deviation
T (blank)	1.000	0.33
T (20Zn)	0.5714	0.25
T (40Zn)	0.8333	0.49
T (30Al)	0.8571	0.21
T (20Zn + 20Al)	0.5238	0.24

Table 3 Corrosion potential (E_{corr}) and corrosion current density (i_{corr}) of oxide films formed on CS in different solutions at 290 °C

	OCP (V)	E_{corr} (V)	i_{corr} (A cm^{-2})
T (blank)	−0.531	−0.540	5.085×10^{-8}
T (20Zn)	−0.118	−0.121	4.826×10^{-9}
T (40Zn)	−0.356	−0.357	1.310×10^{-8}
T (30Al)	−0.674	−0.681	4.948×10^{-8}
T (20Zn + 20Al)	−0.348	−0.349	7.035×10^{-9}

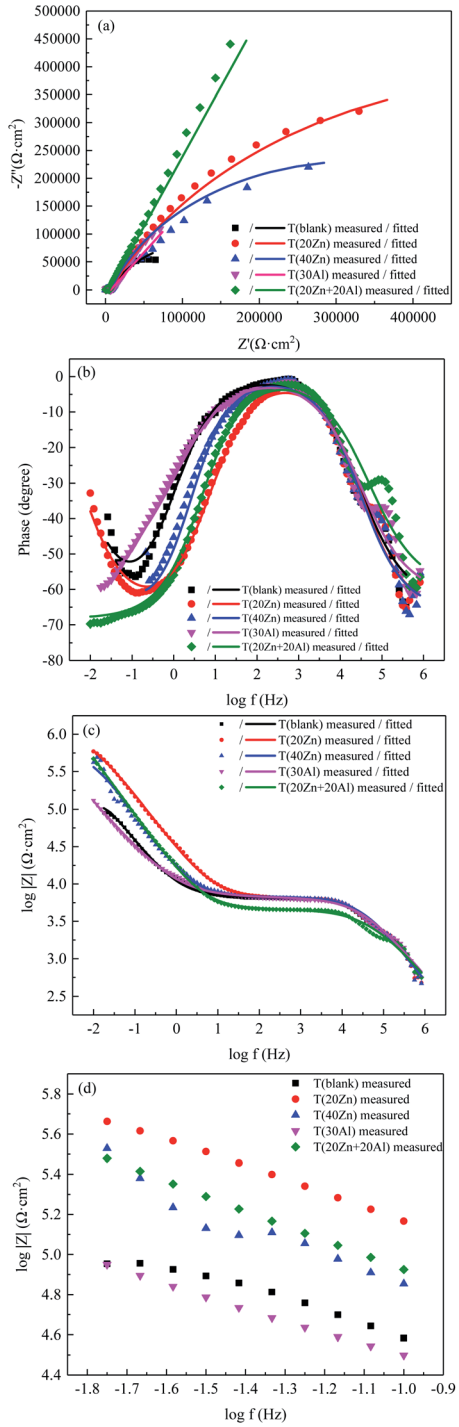

Fig. 2 EIS spectra of oxide films formed on CS in different solutions at 290 °C (dots for measured results in experiments and lines for fitted data by software) (a) Nyquist plots (b) phase angle plots (c) Bode plots (d) Bode plots at low frequency.

Several circuit models were attempted to fit the above experimental data. The best agreement between experimental and fitted data (shown in Fig. 2) was obtained with the equivalent circuit model illustrated in Fig. 3. In the equivalent circuit model, R_s represents the resistance of solution, R_{out} and Q_{out} are the resistance and constant phase element (CPE) of outer oxide

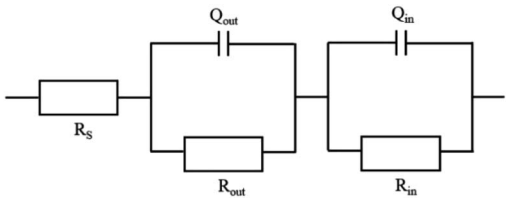

Fig. 3 Electrochemical equivalent circuit mode.

films with respect to the oxide/solution interface, R_{in} and Q_{in} are the resistance and CPE of inner oxide film the oxide/metal interface. Each parameter of circuit elements was fitted in Table 4.

It was obvious that all ion injection treatments increased the resistance of the oxide films formed on CS showing better corrosion resistance. This behavior was also confirmed in the potentiodynamic polarization measurements. The values of R_{in} were much larger than R_{out} in each group and were larger than those of T (blank), which demonstrated the corrosion processing was mainly controlled by the charge transfer at the interface of the inner oxide/metal layer. It was worth noting that the inner resistance increased sharply when Al^{3+} added into simulated primary circuit water, at the same time the aluminum ion as corrosion inhibitor to improve the corrosion resistance of inner structure of oxide films were verified.

Because of the dispersion effect of electric double layer capacitor, for the description of a frequency independent phase shift between the applied AC potential and its current response, CPE which has non-integer power dependence on frequency, was employed and the impedance of CPE was given by the following equation eqn (3):

$$Z = \frac{(j\omega)^{-n}}{Y_0} \quad (3)$$

where Y_0 and n $(0 < n < 1)$ are the parameters of CPE. CPE (Q) was commonly used to represent the capacitances of oxide layer to account for the deviation from the ideal capacitive behavior due to surface inhomogeneity, roughness and adsorption effects.[19,20] Based on the results of electrochemical impedance spectroscopy, a positive trend in the anticorrosive nature of oxide films were indicated by simultaneous injection of zinc and aluminum into high temperature primary circuit water.

3.4 Mott–Schottky analysis

The passive film as suggested by Chao *et al.* contains a high concentration of point defect such as metal vacancies, electrons and holes.[21] Mott–Schottky test is one of the main methods to investigate the semiconductor properties of oxide films.[22] The relationship between the space charge capacitance (C) and the potential (E) of oxide film in electrolyte solution can be described by Mott–Schottky equation, for n-type and p-type semiconductor are eqn (4) and (5) respectively:

$$\frac{1}{C^2} = \frac{2}{\varepsilon\varepsilon_0 e N_d}\left(E - E_{fb} - \frac{KT}{e}\right) \quad (4)$$

Table 4 Fitting parameters of EIS spectra

		Q_{out}		
Group	R_s (Ω cm^{-2})	Y_{out} (S sec^n cm^{-2})	n_{out}	R_{out} (Ω cm^{-2})
T (blank)	4.28×10^{-4}	2.677×10^{-8}	0.7093	6.632×10^{3}
T (20Zn)	1.63×10^{-5}	1.866×10^{-8}	0.7369	6.569×10^{3}
T (40Zn)	2.39×10^{-5}	1.906×10^{-8}	0.7355	6.770×10^{3}
T (30Al)	6.78×10^{-4}	3.589×10^{-8}	0.6846	6.641×10^{3}
T (20Zn + 20Al)	1.1×10^{-3}	6.32×10^{-8}	0.6393	1.209×10^{4}

	Q_{in}		
Group	Y_{in} (S sec^n cm^{-2})	n_{in}	R_{in} (Ω cm^{-2})
T (blank)	3.789×10^{-5}	0.7531	2.614×10^{5}
T (20Zn)	8.875×10^{-6}	0.7434	1.145×10^{6}
T (40Zn)	1.677×10^{-5}	0.7935	6.420×10^{5}
T (30Al)	4.654×10^{-5}	0.6382	1.206×10^{13}
T (20Zn + 20Al)	1.143×10^{-5}	0.7798	1.260×10^{17}

$$\frac{1}{C^2} = -\frac{2}{\varepsilon\varepsilon_0 e N_a}\left(E - E_{fb} - \frac{KT}{e}\right) \quad (5)$$

where C is the space charge capacitance of oxide film, ε_0 is the vacuum dielectric constant ($\varepsilon_0 = 8.85 \times 10^{-14}$ F cm^{-1}), ε is the dielectric constant of semiconductor ($\varepsilon = 12$), e is the electron charge ($e = 1.602 \times 10^{-19}$ C), N_d/N_a is the donor/acceptor density, E is the electrode potential, E_{fb} is the flat band potential, K is the Boltzmann constant ($K = 1.38 \times 10^{-23}$ J K^{-1}), T is the temperature. C^{-2} is linear with the potential E, in consequence, the semiconductor type of oxide film formed on the metal can be judged based on the positive (n-type) or negative (p-type) tangent slope. The donor/acceptor density and flat band potential can be calculated through Mott–Schottky equation.

MS plots of carbon steel samples with oxide films obtained in different Zn^{2+} and Al^{3+} injection conditions were shown in Fig. 4. The test potential was in the range of −1000 mV to +1200 mV and the test solution was 1 ppm LiOH solution at room temperature. The variation of C^{-2} with the applied potential was typical of an n-type semiconductor. The carrier concentration (N_d) and flat band potential (E_{fb}) calculated were listed in Table 5.

The N_d of oxide film formed in 20 ppb Zn^{2+} solution (5.37×10^{16} cm^{-3}) was the lowest among all groups, which was approximately 25.6% of N_d of T (blank) (2.10×10^{17} cm^{-3}). The reduction of the carrier concentration varied in degrees compared to T (blank) after Zn^{2+} and/or Al^{3+} injected into high temperature water. Furthermore, the flat band potential (E_{fb}) had a negative shift with all treatment of solution compared to T (blank) (−0.14 V *vs.* SCE). It has been reported that Zn^{2+} in the spinel structure can reduce the defects which may inhibit the transportation of ions from the metal to solution and minimize the corrosion rate. From the results in Mott–Schottky tests, it can be concluded that the corrosion resistance and the stability of the passive film was improved, and the improvement may be due to the changes in the composition of oxide films formed on carbon steel in different conditions. In the next parts, the composition was analyzed by different methods.

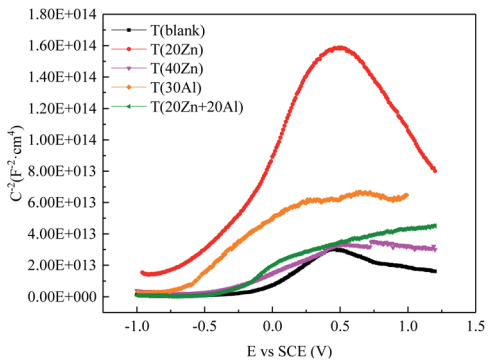

Fig. 4 Mott–Schottky curves of oxide films formed on CS in different Zn^{2+} and Al^{3+} injection conditions.

3.5 Morphology analysis (SEM)

Based on the results of all samples in above analysis, carbon steels in T (20Zn) and T (20Zn + 20Al) had better corrosion resistance than other groups in general. In this study, morphology and composition analysis (SEM + EDS mapping) of oxide films were carried out and shown in Fig. 5 and 6.

Table 5 The carrier concentration (N_d) and flat band potential (E_{fb}) of oxide films formed on CS in different Zn^{2+} and Al^{3+} injection conditions

Group	Semiconductor type	N_d (cm^{-3})	E_{fb} (V)
T (blank)	n	2.10×10^{17}	−0.14
T (20Zn)	n	5.37×10^{16}	−0.43
T (40Zn)	n	3.42×10^{17}	−0.46
T (30Al)	n	1.76×10^{17}	−0.79
T (20Zn + 20Al)	n	1.73×10^{17}	−0.32

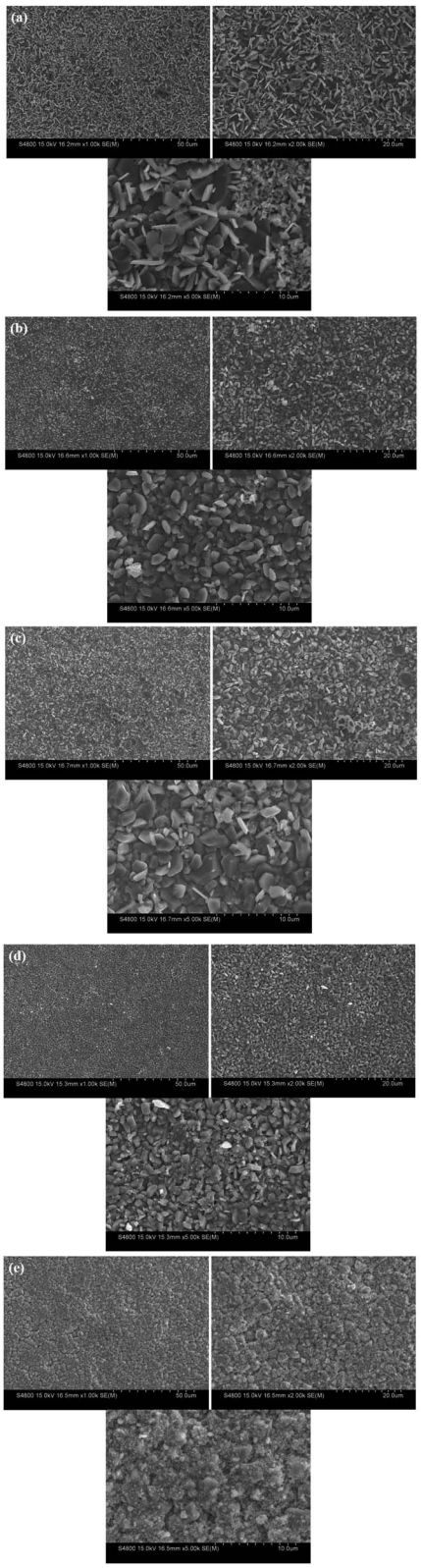

Fig. 5 SEM images of oxide films formed on CS in different conditions (a) T (blank) (b) T (20Zn) (c) T (40Zn) (d) T (30Al) (e) T (20Zn + 20Al).

The loose surface morphology with flaky crystals can be observed on the carbon steel samples corroded in simulated primary circuit coolant at high temperature without zinc and aluminum (as shown in Fig. 5(a)), which mean CS had poor corrosion resistance in lithium hydroxide solution. The average size of particles was approximately 3.1 μm.

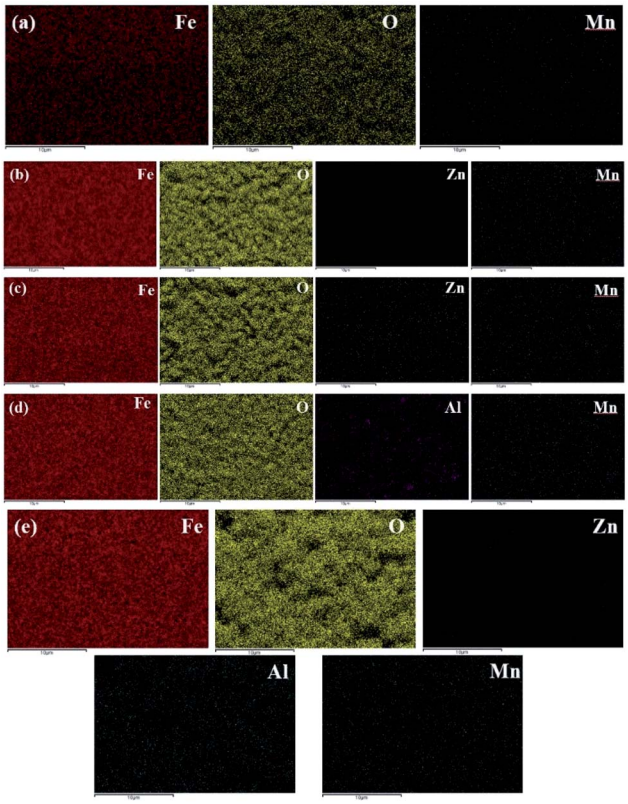

Fig. 6 EDS mapping images of oxide films formed on CS in different conditions (a) T (blank) (b) T (20Zn) (c) T (40Zn) (d) T (30Al) (e) T (20Zn + 20Al).

After using zinc and/or aluminum treatment, the surface of oxide films formed on carbon steels displayed different morphologies (as shown in Fig. 5(b)–(f)). The surface became denser and smoother in varying degrees, and at the same time, many regular tetrahedral and octahedral crystals were observed. With the increase of Zn^{2+} concentration, the surface morphologies were different and the average size of particles were also increased, for which about 1.8 μm in T (20Zn) and 2.4–2.5 μm in T (30Zn) and T (40Zn). Combined with the above electrochemical test results, it was implied that smaller size and denser oxide particles would be useful to improve the corrosion resistance of carbon steel. The average size of particles in T (30Al) were 1.5 μm and the surface of oxide films seems denser than T (20Zn), however the corrosion resistance was not significantly improved due to the results in potentiodynamic polarization analysis. It may be due to different composition of oxide films when Zn^{2+} or Al^{3+} injected into solution.

The EDS mapping of Zn and Al were detected in oxide films (as showed in Fig. 6(b)–(f)), indicating that Zn^{2+} and Al^{3+} in the solution reacted with carbon steels in high temperature conditions. Zinc and aluminum appeared simultaneously in the oxide films of T (20Zn + 20Al) could be attributed to the replacement of part of zinc by aluminum so as to participate in

the formation of oxide films. It can be speculated according to the previous researches,[18,22] zinc ferrite ($ZnFe_2O_4$), $FeAl_2O_4$ and zinc aluminate ($ZnAl_2O_4$) were generated in the treatment of zinc, aluminum and zinc + aluminum respectively, which changed the corrosion resistance of carbon steels.

3.6 XPS analysis

In order to determine the valence state and existence form of different elements in the oxide films, XPS analysis was performed for each sample. The XPS spectra of Fe2p, Mn2p, Zn2p, Al2p and O1s of T (blank), T (20Zn), T (40Zn) and T (20Zn + 20Al) were shown in Fig. 7. The binding energy of each element was corrected using the C1s peak from residual carbon (284.8 eV). The atomic ratio was listed in Table 6.

It has been reported that the peak of Fe $2p_{3/2}$ and Fe $2p_{1/2}$ for iron oxides were 710.6–711.2 eV and 723.2–724.8 eV, respectively. The existence of satellite peak located at 719 eV and 733 eV indicated the Fe^{3+} in oxide films. In general, the peak area of iron was the maximum among the metal elements, that is, iron was the main component in the oxide film. Considering the experimental condition and reaction process, it was judged

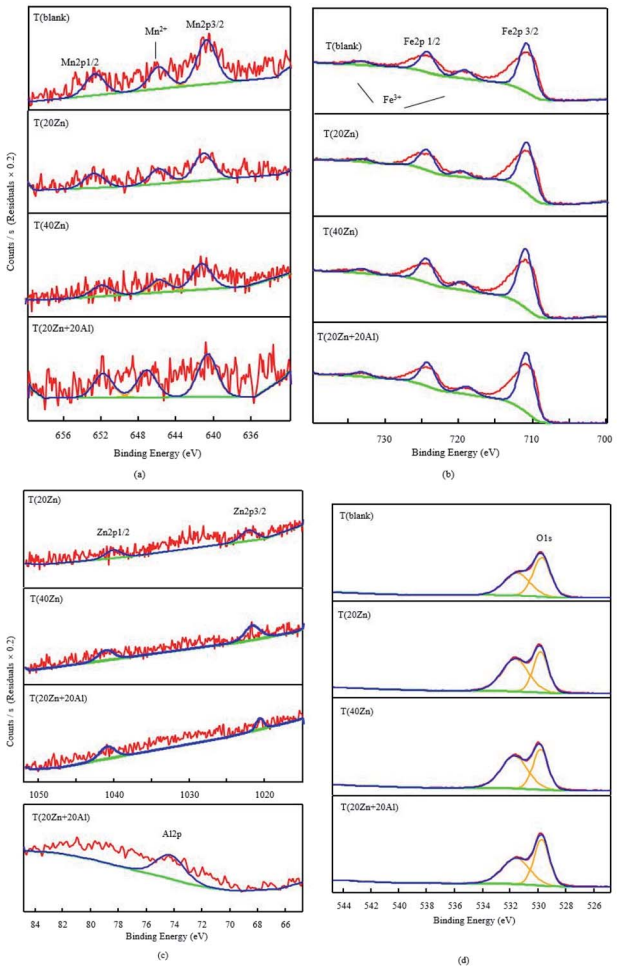

Fig. 7 XPS spectra of Fe2p, Mn2p, Zn2p, O1s and Al2p (a) Mn2p (b) Fe2p (c) Zn2p and Al2p (d) O1s.

Table 6 The atomic ratio of each element in oxide film

	Atomic (%)			
	T (blank)	T (20Zn)	T (40Zn)	T (20Zn + 20Al)
O	49.14	51.54	50.41	40.62
Fe	33.70	26.63	29.37	36.35
Mn	17.16	12.46	12.15	15.9
Zn	—	9.37	8.06	4.92
Al	—	—	—	2.2

that iron oxides (FeO, Fe_2O_3 and Fe_3O_4) are the main substances in T (blank). With the addition of Zn^{2+} and/or Al^{3+} the ratio of satellite peak increased, the content of Fe^{3+} increased, it may be accompanied by the generation of $ZnFe_2O_4$.[23,24]

The Mn2p spectra consisted of $Mn2p_{3/2}$ (~641 eV) and $Mn2p_{1/2}$ (~652 eV) with an additional satellite peak at approximate 646–647 eV, which confirmed the presence of Mn^{2+} state (MnO or $MnFe_2O_4$) in the oxide films.[25] According to the XPS survey scan of each specimen in Table 6, after Zn^{2+} added into solution, the percentage of Mn decreased from 17% to 12%, which may be due to the replacement of Mn^{2+} ($MnFe_2O_4$) by Zn^{2+} ($ZnFe_2O_4$).

Fig. 7(c) showed the XPS spectra in the Zn2p region for samples, zinc species could be detected in the oxide film in zinc and zinc–aluminum treatment groups. The Zn2p core level spectrum for oxide films showed a doublet, whose peak at the binding energy of ~1022 eV and ~1041 eV. The $Zn2p_{3/2}$ and $Zn2p_{1/2}$ binding energy positions revealed the oxidation of Zn atoms and Zn^{2+} chemical state, which may be ZnO and some zinc-containing spinel oxides. The $Zn2p_{1/2}$ at 1044.8 eV in spectra was in great agreement of the value of $ZnAl_2O_4$ in database, indicating the generation of $ZnAl_2O_4$ in T (20Zn + 20Al).

From the spectra of Al2p, aluminum was detected in the oxide film of T (20Zn + 20Al) according to the peak at ~74.1 eV, which proved the form of Al^{3+} and the substance may be Al_2O_3 (74.1 eV) and $ZnAl_2O_4$ (74.0 eV).[26,27] The O1s signal can be fitted with two peaks, respectively due to lattice O^{2-} (529.84 eV) and surface-adsorbed oxygen ions (532 eV). Moreover, it has been reported that ZnO has an unusual O1s spectrum with two peaks possibly indicating either $Zn(OH)_2$ or oxygen vacancies.[28]

3.7 Photocurrent responses

Photoelectrochemical response technology has been widely applied to investigate the passive film on the alloy surface. It can not only analyze the semiconductor property and electronic structure of passive films, but also obtain the composition of the materials in the oxide film qualitatively through calculation.

Photocurrent response tests of the oxide film formed on carbon steel were measured to further probe the effects of zinc and aluminum injection on the composition of the oxide film in primary circuit water of heavy water reactors. Fig. 8 presented the photocurrent response spectrums of oxide films formed in different conditions. All the spectrums exhibited the property of

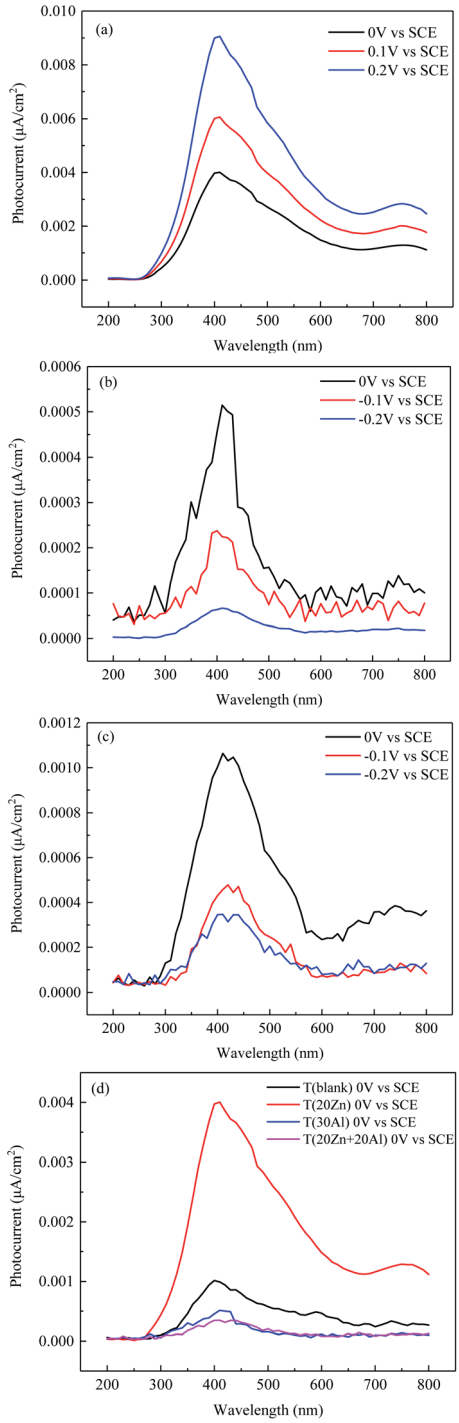

Fig. 8 Photocurrent response spectrum of oxide films formed on CS in different conditions (a) T (20Zn) (b) T (30Al) (c) T (20Zn + 20Al) (d) 0 V *vs.* SCE for different conditions.

n-type semiconductor according to the positive value of photocurrent, these were in consistent with the results of Mott–Schottky tests above. The photocurrent in Fig. 8(a)–(c) increased with the increase of potential and a highest positive peak can be seen at 410 nm. It was shown obviously in Fig. 8(d) that the values of photocurrent in T (30Al) and T (20Zn + 20Al) was much smaller than those of T (20Zn). For implantation of different ions, the photocurrent value fluctuated with the change of wavelength and difference between peaks and valleys were present.

In order to explore the composition of oxide films formed on carbon steel samples, the band gap energy (E_g) of different semiconductor materials was calculated by eqn (6):[29–32]

$$\left(i_{ph} \cdot \frac{h\nu}{I_0}\right)^{1/2} = A\left(h\nu - E_g\right) \quad (6)$$

where i_{ph} is the photocurrent, $h\nu$ is the energy of the incident light, I_0 is the intensity of the light, E_g is the band gap and A is a constant. The light intensity (I_0) at the position of the working electrode was measured at different wavelength in 1 ppm LiOH solution before the experiments. The distribution of light intensity was shown in Fig. 9. Based on the calculation eqn (6), the curves of $(i_{ph} \cdot h\nu/I_0)^{1/2}$ *via* $h\nu$ shown in Fig. 10 indicated that the oxide film formed in high temperature solution with Zn^{2+} and/or Al^{3+} were composed of multiple components. The band gap values of substances in oxide films fitting were listed in Table 7, reference values from literatures also can be seen in Table 7 for comparison.

Combined with the EDS mapping and XPS results shown in Fig. 6(a), iron oxides were the main corrosion products in T (blank) and the atomic percentage ratio of Fe/O was close to 0.7, which implied the substance may be the mixture of magnetite (Fe_3O_4), hematite (Fe_2O_3) and FeO. In addition, due to the presence of manganese in carbon steel matrix, MnO and $MnFe_2O_4$ were also formed in high temperature environment. With the injection of Zn^{2+} into LiOH solution, FeO, Fe_2O_3, MnO, ZnO and $ZnFe_2O_4$ were the main composition of oxide films formed on carbon steel samples. It has been confirmed that $ZnFe_2O_4$ has low solubility and Gibbs free energy and could be preferentially formed in high temperature water and deposited on the surface of metal materials.[44] Therefore, samples in T (20Zn) showed superior corrosion resistance. When the solution only had aluminum ions, $FeAl_2O_4$ was generated in oxide films. After Zn^{2+} and Al^{3+} simultaneously injected in solution, a new substance of $ZnAl_2O_4$ was formed in the oxide film, which were considered to improve the stability and corrosion resistance of carbon steels.

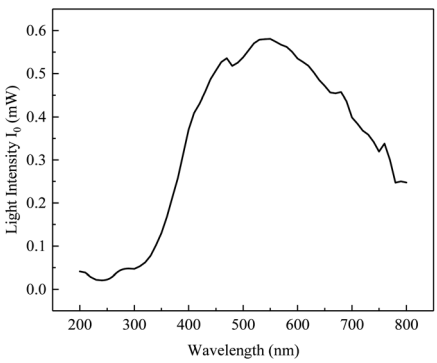

Fig. 9 The distribution of light intensity at the position of the working electrode in different wavelength.

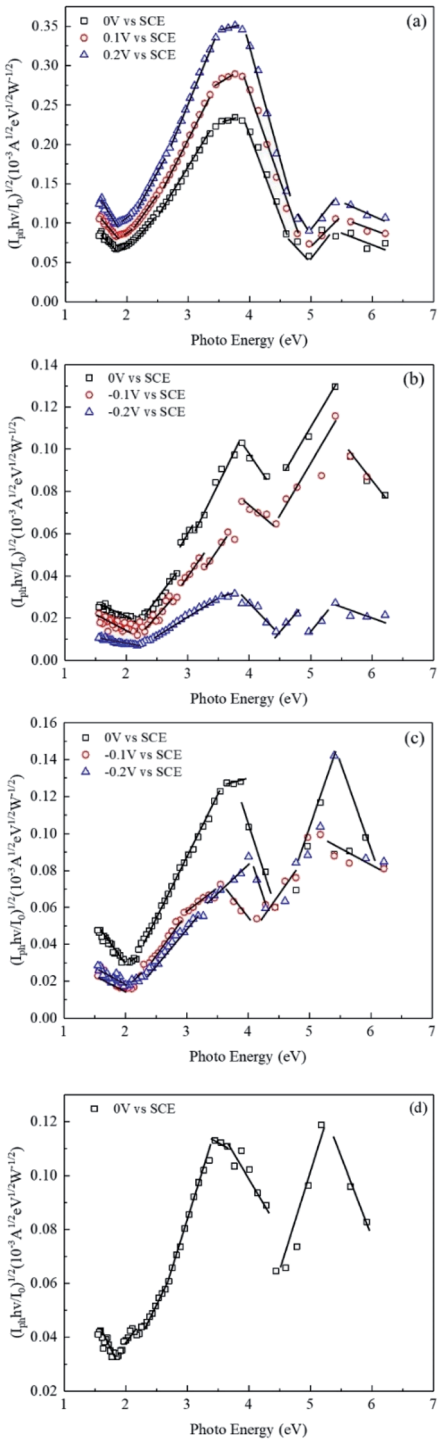

Fig. 10 $(i_{ph}\cdot hv/I_0)^{1/2}$ *via* photo energy for oxide films formed on CS in different conditions. (a) T (20Zn) (b) T (30Al) (c) T (20Zn + 20Al) (d) T (blank).

4 Discussion

The corrosion rate calculated by gravimetric method showed the lowest corrosion rate of T (20Zn + 20Al). Although the rate of T (20Zn) was slightly higher than the lowest value, the difference between these two groups was not obvious. From the polarization plots, the corrosion current density (i_{corr}) of T (20Zn) was lower than that of other treatments. This result was consistent with that of Mott–Schottky tests. The smallest value of donor density (N_d) in T (20Zn) indicated the superior corrosion resistance of oxide films formed on carbon steel. Consequently, 20 ppb Zn^{2+} added into primary circuit coolant of heavy water reactor can significantly enhance the corrosion resistance of A106B carbon steel. For the group T (20Zn + 20Al), although the inner resistance of oxide films from EIS results was too high than other groups, the improvement of corrosion resistance of zinc–aluminum simultaneous injection was close to sole zinc treatment.

Table 7 E_g of substances obtained from linear fitting in different conditions[33–43]

	Fitting E_g (eV)				
Substance	T (20Zn)	T (30Al)	T (20Zn + 20Al)	T (blank)	Reference E_g (eV)
FeO	2.4	2.4	2.4	2.3–2.4	2.3–2.4
Fe_2O_3	2.2	2.1	2.2	2.1–2.2	2.1–2.2
$ZnFe_2O_4$	1.8	—	1.8	—	1.8–1.9
ZnO	3.2–3.6	—	3.2–3.6	—	3.2–3.6
$ZnAl_2O_4$	—	—	3.85	—	3.8–3.9
$FeAl_2O_4$	—	1.78	1.78	—	1.78
MnO	3.9–4.0	4.0	3.6–4.0	3.6–4.0	3.6–4.0
$MnFe_2O_4$	1.76	1.76	1.76	1.76	1.76

Morphology analysis (SEM images) of different ions injection displayed different surface of oxide films but were more compact compared with T (blank). According to the EDS mapping, XPS results and photocurrent response data, it was assumed that $MnFe_2O_4$, $ZnFe_2O_4$, $FeAl_2O_4$ and $ZnAl_2O_4$ were generated in the oxide films. Therefore, the corrosion resistance of oxide films formed on carbon steels can be improved by modifying the composition through metal cation ions added into primary circuit coolant in heavy water reactors.

Based on the equivalent circuit model in Fig. 3, the mathematics expression of the impedance of electrode system could be written as eqn (7):

$$Z = R_S + \frac{1}{\frac{1}{R_{out}} + Y_{out}(jw)^{n_{out}}} + \frac{1}{\frac{1}{R_{in}} + Y_{in}(jw)^{n_{in}}} \quad (7)$$

The values of n_{out} and nin in the range of 0.5–1 were associated to the heterogeneity and complexity of electrode surface.[45] The n value was away from 1 which indicated the presence of a non-homogeneous surface of the oxide film. Data from Fig. 2(c) showed the linear slope of was close to −1, which implied the typical capacitive behavior of passive films in all treatments of carbon steels. Oxide films formed in the presence of Zn^{2+} and/or Al^{3+} showed increased capacitive loop which could be related to increase in protectiveness of oxide.[46] At low frequencies, the phase angle increased also implied the increment of capacitance. Moreover, the resistance R_{in} corresponding to the oxide/metal interface increased to $1.26 \times 10^{17}\ \Omega\ cm^{-2}$

and n_{in} value of 0.7798 indicated that the thickening of the oxide film improved the film passivity in T (20Zn + 20Al). It was speculated that the composition of the oxide film has been changed after aluminum ion implantation, but this composition has little contribution to improving the corrosion resistance of carbon steel in primary circuit water of CANDU.

Zinc ferrite ($ZnFe_2O_4$), manganese ferrite ($MnFe_2O_4$), hercynite ($FeAl_2O_4$) and zinc aluminate ($ZnAl_2O_4$) are common spinel with the structure of one-eighth of the tetrahedral and one-half of the octahedral interstices filled by cations. Without zinc treatment, magnetite (Fe_3O_4) and $MnFe_2O_4$ formed on the surface of carbon steels. After zinc injected into primary circuit coolant, along with the Fe^{3+} and Mn^{2+} ions at tetrahedral sites were progressively replaced by Zn^{2+}, spinel-type oxide of $ZnFe_2O_4$ were generated. With only Al^{3+} in high temperature solution, spinel-structure $FeAl_2O_4$ formed on carbon steels. When zinc and aluminum were simultaneously injected, Zn^{2+} replaced Fe^{2+} of $FeAl_2O_4$ and Al^{3+} replaced Fe^{3+} of $ZnFe_2O_4$ and preferentially produced $ZnAl_2O_4$. The corrosion resistance of carbon steel was significantly enhanced because of the generation of $ZnFe_2O_4$ with zinc treatment.

Obviously, although the content of manganese in carbon steel was not too much compared to iron, the manganese oxide and manganese ferrite formed in high temperature water environment also changed with the injection of Zn^{2+}. Cao *et al.* point out that the difference in deoxidization degree played an important role in the corrosion resistance of carbon steel. The inclusion of potato-like manganese oxide and olive-like sulfide in boiling steel was the reason for its weaker pitting induction sensitivity and lower pitting corrosion growth rate.[47] Moreover, manganese used in steel have higher affinities for oxygen than iron. It is clear that even though small amounts of these elements are present in the steel they still have a higher affinity for oxygen than iron.[48] In this study, the changes in the total content of manganese and zinc in oxide films based on XPS results were analyzed deeply. Fig. 11 showed the relationship between corrosion current density (i_{corr}) and the content of Mn + Zn. In T (20Zn) the total content of Mn and Zn reached the highest value (21.83%), and at the same time the corrosion current density behaved the lowest value which indicated the best corrosion resistance among different ion concentration treatments. Therefore, for enhance the corrosion resistance and improve the stability of carbon steel, suitable concentration Zn^{2+} was worth noting, but not as much as possible.

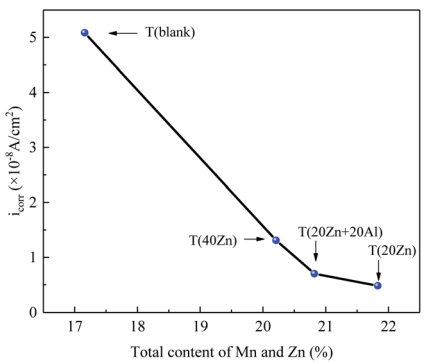

Fig. 11 The relationship between i_{corr} and total content of Mn and Zn.

5 Conclusions

The corrosion behavior and semiconductor property of oxide films formed on A106B carbon steel were investigated in this study. Oxidation was carried out in simulated primary circuit coolant (LiOH solution) of heavy water reactors. The effect of zinc/aluminum treatment and zinc–aluminum simultaneous injection on the corrosion resistance of oxide films were analyzed.

Compared with T (blank), all the implantation can reduce corrosion rate of carbon steels. The oxide film on the surface of carbon steel all behaved n-type semiconductor properties. For different Zn^{2+} and Al^{3+} concentration, T (20Zn) and T (20Zn + 20Al) behaved denser surface and better corrosion resistance than other groups. New spinel phases of $ZnFe_2O_4$, $FeAl_2O_4$ and $ZnAl_2O_4$ formed in oxide films enhance the stability and corrosion resistance of carbon steels. In consequence, the oxide film formed with 20 ppb Zn^{2+} had the highest total content manganese and zinc, the lowest corrosion current density and the best corrosion resistance. Compared with T (20Zn), zinc–aluminum simultaneous injection treatment can also enhance the corrosion resistance to a greater extent, but the effect was not much different than that of zinc injection alone.

Conflicts of interest

There are no conflicts to declare.

Acknowledgements

This study was financially supported by the Natural Science Foundation of Beijing Municipality, China (Grant No. 2192051).

References

1 R. L. Tapping, Materials performance in CANDU reactors: The first 30 years and the prognosis for life extension and new designs, *J. Nucl. Mater.*, 2008, **383**(1–2), 1–8.
2 S. Zhang, R. Shi and Y. Tan, Comparison of the Solubility of ZnFe2O4, Fe3O4 and Fe2O3 in High Temperature Water, *J. Solution Chem.*, 2018, **47**(6), 1112–1126.
3 V. Malinovschi, C. Ducu, N. Aldea, *et al.*, Study of carbon steel corrosion layer by X-ray diffraction and absorption methods, *J. Nucl. Mater.*, 2006, **352**(1), 107–115.
4 H. Subramanian, V. Subramanian, P. Chandramohan, *et al.*, Role of magnesium ions in reducing high temperature aqueous corrosion of carbon steel, *Corros. Sci.*, 2013, **70**(3), 127–139.
5 Y. F. Cheng, J. Bullerwell and F. R. Steward, Electrochemical investigation of the corrosion behavior of chromium-modified carbon steels in water, *Electrochim. Acta*, 2003, **48**, 1521–1530.
6 H. Subramanian, P. Madasamy, V. S. Sathyaseelan, *et al.*, Corrosion of carbon steel feeders during dilute chemical

decontamination of primary heat transport system of PHWRs, *Mater. Corros.*, 2012, **63**(1), 29–35.

7 D. Lister and S. Uchida, Determining water chemistry conditions in nuclear reactor coolants, *J. Nucl. Sci. Technol.*, 2015, **52**(4), 451–466.

8 S. Uchida and Y. Katsumura, Water chemistry technology – one of the key technologies for safe and reliable nuclear power plant operation, *J. Nucl. Sci. Technol.*, 2013, **50**(4), 346–362.

9 V. Subramanian, S. Chandran, H. Subramanian, *et al.*, Electrochemical characterization of oxide formed on chromium containing mild steel alloys in LiOH medium, *Mater. Chem. Phys.*, 2014, **145**(3), 499–509.

10 M. K. Kumar, K. Gaonkar, S. Ghosh, *et al.*, Optimization of the hot conditioning of carbon steel surfaces of primary heat transport system of Pressurized Heavy Water Reactors using electrochemical impedance spectroscopy, *J. Nucl. Mater.*, 2010, **401**(1–3), 46–54.

11 G. Li, Z. Liang and X. Yang. Corrosion Susceptibility in High Temperature Liquid/Vapor Environments of Materials for Tubing of Heavy-Water Collection System in *CANDU Nuclear Power Plant[C]//International Conference on Nuclear Engineering*. 2017.

12 L. Huang, K. Wang, W. Wang, *et al.*, Mechanical and corrosion properties of low-carbon steel prepared by friction stir processing, *Int. J. Miner., Metall. Mater.*, 2019, **26**, 202–209.

13 L. Zhang, K. Chen, J. Wang, *et al.*, Effects of zinc injection on stress corrosion cracking of cold worked austenitic stainless steel in high-temperature water environments, *Scr. Mater.*, 2017, **140**, 50–54.

14 J. A. Sawicki and H. A. Allsop, Evidence of zinc ferrite formation on carbon steel in primary-side coolant with added soluble zinc, *J. Nucl. Mater.*, 1996, **240**(1), 22–26.

15 Z. H. Walker and H. A. Allsop, *et al.*, Effects of Zn addition under CANDU pressurized heavy water reactor conditions. *Seventh International Conference of Water Chemistry of Nuclear Reactor*, 1996.

16 S. Zhang, C. Sun and Y. Tan, Influence of Zinc and Aluminum Simultaneous Injection on Corrosion Behavior and Semiconducting Properties of Oxide Film on 304L, *Int. J. Electrochem. Sci.*, 2020, 9874–9887.

17 S. Zhang, R. Shi, Y. Chen and M. Wang, Corrosion behavior of oxide films on AISI 316L SS formed in high temperature water with simultaneous injection of zinc and aluminum, *J. Alloys Compd.*, 2018, **731**, 1230–1237.

18 S. Zhang, C. Sun and Y. Tan, Corrosion Behavior of High-Strength Low-Alloy Steel in High-Temperature Water with Zinc and Aluminum Simultaneous Injection, *Corrosion*, 2020, **76**(10), 918–929.

19 C. Lei, X. Chen, Y. Li, Y. Chen and B. Yang, Enhanced corrosion resistance of SA106B low-carbon steel fabricated by rotationally accelerated shot peening, *Metals*, 2019, **9**, 872.

20 B. Cox, *et al.*, Simulating porous oxide films on zirconium alloys, *J. Nucl. Mater.*, 1995, **218**(3), 324–334.

21 C. Y. Chao, L. F. Lin and D. D. Macdonald, A point defect model for anodic passive films, *J. Electrochem. Soc.*, 1981, **128**(6), 1187–1194.

22 Y. Lan, Z. Liu, Z. Guo, *et al.*, A promising p-type Co-ZnFe2O4 nanorods film as photocathode for electrochemical water splitting, *Chem. Commun.*, 2020, **56**(39), 5279–5282.

23 J. Han, Y. Lan, Q. Song, *et al.*, Zinc ferrite-based p–n homojunction with multi-effect for efficient photoelectrochemical water splitting, *Chem. Commun.*, 2020, **56**(86), 13205–13208.

24 Si-H. Do, Y.-J. Kwon, *et al.*, Persulfate reactivity enhanced by Fe2O3-MnO and CaO-Fe2O3-MnO composite: Identification of composite and degradation of CCl4 at various levels of pH, *Chem. Eng. J.*, 2013, **221**, 71–80.

25 X. Peng, J. Qu, S. Tian, Y. Ding, X. Hai, B. Jiang, M. Wu and J. Qiu, Green fabrication of magnetic recoverable graphene/MnFe2O4 hybrids for efficient decomposition of methylene blue and the Mn/Fe redox synergetic mechanism, *RSC Adv.*, 2016, **6**, 104549.

26 J. Shi, Preparation and properties of spinel $ZnAl_2O_4$ nanoparticles, Master thesis, Lanzhou University of Technology, 2019.

27 X. Wu, Studies on preparation and properties of transition metal doped spinel $ZnAl_2O_4$ nanomaterials, Doctoral dissertation, Lanzhou University of Technology, 2018.

28 J. C. Ding, H. Y. Li, Z. X. Cai, *et al.*, Near room temperature CO sensing by mesoporous LaCoO3 nanowires functionalized with Pd nanodots, *Sens. Actuators, B*, 2016, **222**, 517–524.

29 S. Zhang, J. Lian and Y. Tan, Analysis of photocurrent responses of oxide films formed on stainless steel, *Electrochim. Acta*, 2013, **89**, 253–261.

30 N. F. Mott and E. A. Davis, *Electronic Processes in Non-crystalline Materials*, Clarendon Press, Oxford, 2nd edn, 1979.

31 S. Fujimoto and H. Tsuchiya, Semiconductor properties and protective role of passive films of iron base alloys, *Corros. Sci.*, 2007, **49**, 195–202.

32 M. Salem, S. Akir, T. Ghrib, K. Daoudi and M. Gaidi, Fe-doping effect on the photoelectrochemical properties enhancement of ZnO films, *J. Alloys Compd.*, 2016, **685**, 107–113.

33 Y. A. Bratashevskii, A. Y. Zakharov and Y. M. Ivanchenko, Forbidden band width change in semiconductor substitution alloys, *Solid State Commun.*, 1974, **15**(11), 1777–1779.

34 S. Piazza, M. Sperandeo, C. Sunseri, *et al.*, Photoelectrochemical investigation of passive layers formed on Fe in different electrolytic solutions, *Corros. Sci.*, 2004, **46**(4), 831–851.

35 M. Dhiman, R. Sharma, V. Kumar, *et al.*, Morphology controlled hydrothermal synthesis and photocatalytic properties of ZnFe2O4 nanostructures, *Ceram. Int.*, 2016, **42**(11), 12594–12605.

36 P. Manca, A relation between the binding energy and the band-gap energy in semiconductors of diamond or zinc-blende structure, *J. Phys. Chem. Solids*, 1961, **20**(3), 268–273.

37 H. Dixit, N. Tandon, S. Cottenier, *et al.*, Electronic structure and band gap of zinc spinel oxides beyond LDA: ZnAl2O4, ZnGa2O4 and ZnIn2O4, *New J. Phys.*, 2011, **13**(6), 063002.
38 S. K. Sampath, D. G. Kanhere and R. Pandey, Electronic structure of spinel oxides: zinc aluminate and zinc gallate, *J. Phys.: Condens. Matter*, 1999, **11**(18), 3635.
39 H. Mu, Design and synthesis of $FeAl_2O_4$-based visible-light-driven photocatalysts and their photocatalytic properties, Doctoral dissertation, Tianjin University, 2017.
40 D. K. Kanan and E. A. Carter, Band Gap Engineering of MnO *via* ZnO Alloying: A Potential New Visible-Light Photocatalyst, *J. Phys. Chem. C*, 2012, **116**(18), 9876–9887.
41 N. Barakat, K. D. Woo, S. G. Ansari, *et al.*, Preparation of nanofibers consisting of MnO/Mn3O4 by using the electrospinning technique: the nanofibers have two band-gap energies, *Appl. Phys. A: Solids Surf.*, 2009, **95**(3), 769–776.
42 M. A. Bryushinin, A. A. Petrov, R. V. Pisarev, *et al.*, Non-steady-state photoelectromotive force in the wide-band-gap dielectric MnO, *Phys. Solid State*, 2015, **57**(5), 907–913.
43 P. Amalthi, J. J. Vijaya, L. J. Kennedy, *et al.*, Microwave Based Synthesis; Structural, Optical and Magnetic Measurements of Co2+ Doped MnFe2O4, *J. Nanosci. Nanotechnol.*, 2016, **16**, 715–722.
44 R. Shi, Semiconductor electrochemical research on mechanism of corrosion resistance of oxide films on Fe-based alloys, Doctoral dissertation, North Chin Electric Power University, 2018.
45 M. Cai and S. -M. Park, Oxidation of zinc in alkaline solutions studied by electrochemical impedance spectroscopy, *J. Electrochem. Soc.*, 1996, **143**, 3895–3902.
46 O. Sotelo-Mazón, J. Porcayo-Calderon and C. Cuevas-Arteaga, EIS evaluation of Fe, Cr, and Ni in NaVO at 700°C, *J. Spectrosc.*, 2014, 1–10.
47 G. Cao, L. Guoming, W. Chang, *et al.*, Influence of deoxidization on resistance against pitting corrosion of carbon steel, *J. Mater. Eng.*, 2009, **11**, 27–30.
48 P. R. Wilson and Z. Chen, The effect of manganese and chromium on surface oxidation products formed during batch annealing of low carbon steel strip, *Corros. Sci.*, 2007, **49**, 1305–1320.